Geochemical Perspectives Letters

Plagioclase as a magmatic nitrogen reservoir in reduced planetary crusts

Y. Li

Supplementary Information

The Supplementary Information includes:

- Starting materials
- Analyses
- Estimation of sample fO_2
- Equilibrium partitioning
- Tables S-1 to S-4
- Figures S-1 to S-4
- Supplementary Information References

Starting materials

Our starting materials were composed of synthetic silicates and Fe_3N. Major element compositions of the synthetic silicates were similar to those of the lunar magma ocean residual melt after 80% crystallization (Lin *et al.*, 2017) and mid-ocean ridge basalt. The water and FeO_{tot} contents in some silicates were also varied (Table S-1). All synthetic silicates were prepared from high-purity oxides and carbonates as described in (Li *et al.*, 2017). Water was introduced by the addition of $Al(OH)_3$. To minimize the absorbed water contents, the SiO_2, TiO_2, Al_2O_3, and MgO powders were each heated at 1000 °C for 16 h, $CaCO_3$ at 200 °C for 5 h, and the Na_2CO_3 at 110 °C for 5 h. After drying, the weighed oxides and carbonates were mixed and ground in ethanol in an agate mortar for 1 h, and then dried at room temperature. The dried mixture was heated in a muffle furnace at 1000 °C overnight to decarbonate. To limit the introduction of ferric iron into the subsequent partitioning experiments, the FeO powder was finally added to the decarbonated mixture. At this stage, 0.5–1 wt. % H_2O was introduced by the addition of $Al(OH)_3$ into two starting silicates (Table S-1). The other silicates were nominally water-free. The final mixture was then ground again in ethanol in an agate mortar for 1 h and dried at room temperature. All dried silicates were stored in a vacuum oven before loading into sample capsules. Mixed silicate (50 %) and Fe_3N (50 %) powders were loaded into graphite-lined $Pt_{95}Rh_{05}$ capsules. The use of Fe_3N was to ensure the presence of an Fe-rich metallic phase, which, together with the FeO in the silicate melt, buffered the fO_2 below the Fe–FeO buffer, and to assure the saturation of N_2-rich gas as well.

High-pressure experiments

High-pressure experiments were designed to investigate the effects that pressure, fO_2, and silicate composition (including water concentration in the silicate melt) have on N partitioning between plagioclase and silicate melt. The experiments were performed at 0.4–1.5 GPa and 1100–1200 °C in an end-loaded, solid media piston cylinder apparatus, using 3/4-inch diameter talc-Pyrex assemblies with graphite heaters. Pressure was calibrated against the quartz–coesite and kyanite–sillimanite transitions, and a friction correction of 18 % was applied. The pressure uncertainty was estimated to be better than 0.1 GPa. The experimental temperature, measured by S-type ($Pt–Pt_{90}Rh_{10}$) thermocouple, was controlled to ± 2 °C and accurate to ± 10 °C.

At the target pressures, the experimental temperatures were first raised to 100–150 °C higher than the target temperatures and held for ~ 20 min. The temperatures were then lowered to the targe temperatures within 10–15 h. At the target temperatures the experiments lasted 16–32 h. This experimental approach has been used in previous studies for determining plagioclase–silicate melt partitioning of volatiles at conditions similar to those investigated in this study (Lin *et al.*, 2017; Jing *et al.*, 2024). All experiments were terminated by switching off the electrical power supplied to the graphite heaters. The samples were prepared for the analyses using electron microprobe and Fourier transform infrared spectroscopy (FTIR).

Analyses

EPMA: The electron probe microanalysis (EPMA) for composition analysis was carried out at the State Key Laboratory of Geological Processes and Mineral Resources, China University of Geosciences (Wuhan), using a JEOL JXA-iHP200F field emission electron probe equipped with five spectrometers. The samples were carbon-coated according to the method provided by (Zhang and Yang, 2016), with a uniform coating of approximately 20 nm thick carbon film. The analytical procedure for major elements other than N followed the guidelines of (Yang, 2022). The measurement time for the characteristic peaks of Na, Mg, Al, Si, Fe, K, Ca, and Ba elements was 10 s, while the measurement time for Mn and Ti was 20 s. The measurement time for background was half of the peak measurement time. The standard samples used were as follows: jadeite (Na), diopside (Ca, Mg), garnet (Al, Fe), orthoclase (K), olivine (Si), rhodonite (Mn), and rutile (Ti).

N concentrations in plagioclase and silicate melt were measured using two different electron microprobes: JEOL JXA-8230 with an LDE1L diffracting crystal and JEOL JXA-iHP200F with an LDE5H diffracting crystal. Using JEOL JXA-8230 with an LDE1L crystal, the procedures used in (Gao *et al.*, 2022) were followed. The background of light elements, such as N, is not a straight but curved line, which significantly affects the accuracy of N analyses when using the two-point background interpolation method to subtract the background (e.g., Fig. S2 of Gao *et al.* (2022)). To address this issue, previous workers used either an exponential equation or a blank sample to subtract the background (Donovan *et al.*, 2011; Li *et al.*, 2015; Mallik *et al.*, 2018; Cui *et al.*, 2019; von der Handt *et al.*, 2019; Jackson *et al.*, 2021; Gao *et al.*, 2022; Mare *et al.*, 2025). In this study, an exponential equation was used to subtract the N background, through selecting four points on each side of the N peak and fitting them into an exponential equation to obtain the relevant coefficients. The N background and peak counts were measured by using an accelerating voltage of 10 kV, a beam current of 150 nA, 10 µm beam size, and 200 s of counting time. The interference from the Ll peak of Ti with the N Kα peak was corrected by measuring a rutile crystal. BN was used as the standard. These analytical procedures yielded N detection limits of ~350 µg/g (3σ), and 1150 ± 80 µg/g N was measured for a hyalophane feldspar crystal, which is comparable to other measurements on this same feldspar crystal (see below). The validity of this approach was further confirmed by measuring two basaltic glasses with N contents determined by SIMS1280 (MP3 = 250 ± 50 µg/g; MP4 = 160 ± 10 µg/g), which yielded MP3 = 200 ± 90 µg/g and MP4 = 180 ± 50 µg/g.

Using JEOL JXA-iHP200F with an LDE5H crystal, the approach similar to that used in (Jackson *et al.*, 2021) was followed. The N background and peak counts were measured by using an accelerating voltage of 10 kV, a beam current of 100 nA, 10 µm beam size, and 100 s of counting time. An exponential equation was also used to subtract the N background, through selecting four points on each side of the N peak and fitting them into an exponential equation to obtain the relevant coefficients. The interference from the Ll peak of Ti with the N Kα peak was also corrected by measuring a rutile crystal, and the validity of this method was confirmed by measuring a TiN standard. The advantage of LDE5H crystal is its more sensitivity to N compared to LDE1L crystal; however, the use of LDE5H crystal produced a significant "ghost peak" in the background located on the N Kα peak, similar to the observation when using LDE5L crystal as shown in Fig. S1 of Jackson *et al.* (2021). It is found that this ghost peak exists when measuring different metals, oxides, silicate minerals, and silicate glasses, and the peak intensity does not correlate with sample matrix. Shown in Jackson *et al.* (2021), the ghost peak intensities of felsic glasses and feldspar are nearly the same, but the intensity of mica is ~20 % higher. In this study, in four analytical sessions spanning four months in 2025, the peak intensity of a N-free feldspar and a N-free quartz varied from 85 ± 2 cps/100 nA (n=6) to 98 ± 7 cps/100 nA (n=20), with an average of 90 ± 7 cps/100 nA. Using BN as the standard and using these peak intensities to subtract from the measured intensities for the hyalophane feldspar crystal, it yielded N-contents in the range of 1070 ± 70 µg/g (n = 31) to 1150 ± 50 µg/g (n = 20), with an average of 1100 ± 44 µg/g. These measured N-contents are well comparable to the measurements in different studies for this same hyalophane feldspar crystal: 1200 µg/g (Beran *et al.*, 1992), 1130 ± 150 µg/g (Mosenfelder *et al.*, 2019), 900 ± 300 µg/g (Jackson *et al.*, 2021), and 930 µg/g (Yang *et al.*, 2022). Following these prior tests, the ghost peak intensities of the N-free quartz were used to subtract from the measured intensities to calculate N-contents in all samples in this study. N-contents of all samples and standards were corrected for matrix effect by ZAF. Under 3σ conditions, the detection limit was ~200 µg/g.

Figure S-4 shows a comparison in N concentrations in both plagioclases and silicate melt measured using JEOL JXA-8230 with an LDE1L crystal and JEOL JXA-iHP200F with an LDE5H crystal. These two different methods yielded nearly identical results within uncertainties, but the data measured using LDE5H crystal appear to be systematically, slightly higher than those measured using LDE1L crystal.

Fourier transform infrared (FTIR) spectroscopy: Some of the quenched silicate glasses were chosen to determine their water content and N species by using a Bruker VERTEX 70 FTIR. Glass samples were double-side polished with the thicknesses varying between 50 and 300 µm, and then cleaned with acetone before analysis. Spectra were recorded from 600 to 6000 cm^{-1} with 128 scans and a resolution of 4 cm^{-1}. The silicate glasses show typical absorption peaks of 3530 cm^{-1} and 1630 cm^{-1} attributed to water, and 1515 and 1430 cm^{-1} attributed to carbonate. The typical absorption peaks of N–H species, which appear at ~1615 cm^{-1} and ~3370 cm^{-1} (Armstrong *et al.*, 2015; Mosenfelder *et al.*, 2019), were observed. The water content in the glasses was calculated using the Lambert-Beer Law:

$$c\ (\text{wt. \%}) = (1.802 \cdot A) / (d \cdot \rho \cdot \varepsilon) \qquad \text{(Eq. S-1)}$$

where, c, A, d, ρ , and ε refer to the water content in the glass, the absorption intensity or area of the peak at wavenumber ~3550 cm^{-1}, the thickness of the sample (cm, measured using a digital micrometer), the density of the sample (2.819 $g \cdot cm^{-3}$ is used in this study (Yamashita *et al.*, 1997; Hamada *et al.*, 2013)), and the absorption coefficient (64 $l \cdot mol^{-1} \cdot cm^{-1}$ (Yamashita *et al.*, 1997)), respectively.

Estimation of sample fO_2

The fO_2 prevailing during the experiments was calculated from the coexistence of Fe-rich metallic melt and silicate melt using the following equilibrium:

$$FeO\ (\text{silicate melt}) = Fe\ (\text{metallic melt}) + 1/2O_2 \qquad \text{(Eq. S-2)}$$

from which the fO_2 relative to fO_2 of the Fe–FeO buffer, at any given P–T, can be defined as:

$$\Delta IW = 2 \log (a_{FeO}/a_{Fe}) = 2 \log (X_{FeO}\gamma_{FeO}/X_{Fe}\gamma_{Fe}) \quad \text{(Eq. S-3)}$$

a_{FeO} represents the activity of FeO component in the silicate melt; a_{Fe} represents the activity of Fe component in the metallic melt; X_{FeO} and X_{Fe} are the mole fractions of FeO in the silicate melt and Fe in the metallic melt, respectively; γ_{FeO} and γ_{Fe} are the activity coefficients of FeO in the silicate melt and Fe in the metallic melt, respectively. The fO_2 calculation was performed assuming γ_{FeO} = ~1.5 (Holzheid *et al.*, 1997; O'Neill and Eggins, 2002). Activity coefficients of Fe in Fe-rich metallic melt, γ_{Fe}, were calculated using the ε-approach, which takes into account the non-ideal interaction between all the components in the Fe-rich metallic melt (Ma, 2001; Wood *et al.*, 2013). The online "Metal Activity Calculator" (norrisau.org/expet/metalact/) was used to calculate the Fe-activity in the metallic melt. The calculated logfO_2 values of all runs varied between IW−0.7 and IW−1.8 (Table S-2).

Equilibrium partitioning

Several lines of evidence suggest the achievement of equilibrium partitioning in this study. First, mineral–silicate melt show sharp contacts without any resorption textures (Fig. 1). Both plagioclase and silicate melt have small standard deviations for major and minor elements (Tables S-3 and S-4). N concentrations in plagioclase and silicate melt are also homogeneous with small standard deviations (Table S-2). Second, two experiments LMO-4 and LMO-8 were run at the same conditions but with duration ranging from 16 to 32 h. Their N concentrations are identical within uncertainties in plagioclase (480 ± 40 vs. 440 ± 60 µg/g) and silicate melt (2600 ± 210 vs. 2890 ± 100 µg/g) (Table S-2). Third, our experimental duration and approach are well comparable to those of the experiments at similar temperatures for determining volatile (H and F) partitioning between plagioclase, orthopyroxene, and silicate melt using similar starting silicate, where the equilibrium was demonstrated (Lin *et al.*, 2017; Jing *et al.*, 2024). Jackson *et al.* (2021) also showed that equilibrium partitioning of N between minerals and felsic melt may be approached with durations of 24–48 h at IW buffer and 750–775 °C.

Supplementary Tables

Table S-1 The starting silicate composition (in wt. %).

Sample No.	SiO_2	TiO_2	Al_2O_3	FeO	MgO	CaO	Na_2O	H_2O	Total
Sili-A	49.83	1.95	16.29	10.39	9.91	11.63	-	n.w.f	100
Sili-B	52.58	2.06	17.19	5.45	10.45	12.27	-	n.w.f	100
Sili-C	54.95	2.15	17.97	1.19	10.92	12.82	-	n.w.f	100
Sili-D	49.07	1.92	16.04	10.23	9.75	11.45	-	1.0	99.46
Sili-F	49.58	1.95	16.21	10.34	9.85	11.57	-	0.5	100
MORB	50.90	1.26	16.89	7.45	7.56	10.9	4.03	n.w.f	98.99

n.w.f = nominally water-free.

Table S-2 Experimental conditions and products. Table S-2 (.xlsx) is available for download from the online version of this article at https://doi.org/10.7185/geochemlet.2620.

Table S-3 Major and minor elements of the quenched silicate melts (in wt. %).

Run No.	TiO_2	CaO	K_2O	Na_2O	MgO	SiO_2	Al_2O_3	MnO	FeO_{tot}	Total	NBO/T
LMO-1	1.94	10.08	0.03	0.08	6.44	42.45	14.37	0.00	24.82	100.21	1.04
1-σ	0.04	0.07	0.00	0.01	0.37	0.77	0.36	0.01	1.38	0.07	
LMO-3	3.50	11.06	0.05	0.08	6.31	47.79	12.46	0.01	18.37	99.64	0.90
1-σ	0.30	0.19	0.01	0.01	0.36	0.44	0.37	0.01	0.40	0.17	
LMO-4	3.41	9.89	0.07	0.08	4.24	42.45	13.35	0.01	25.37	98.87	1.00
1-σ	0.15	0.09	0.01	0.01	0.10	0.29	0.18	0.01	0.30	0.40	
LMO-6	1.85	10.82	0.04	0.11	7.57	46.28	15.40	0.01	17.42	99.50	0.87
1-σ	0.03	0.08	0.01	0.01	0.07	0.10	0.12	0.01	0.15	0.31	
LMO-8	3.35	10.19	0.06	0.07	4.37	44.08	13.64	0.00	22.59	98.35	0.91
1-σ	0.18	0.08	0.01	0.01	0.11	0.18	0.20	0.01	0.28	0.25	
LMO-9	6.78	11.59	0.13	0.05	5.70	50.85	15.18	0.00	7.99	99.12	0.51
1-σ	0.38	0.10	0.01	0.01	0.14	0.30	0.17	0.00	0.57	0.23	
LMO-11	3.25	11.96	0.05	0.04	5.47	53.02	15.65	0.01	10.08	99.52	0.55
1-σ	0.26	0.13	0.01	0.01	0.20	0.41	0.29	0.01	0.49	0.20	
MORB-3	1.55	6.38	0.38	5.40	4.09	49.15	18.88	0.16	12.86	98.85	0.50
1-σ	0.08	0.10	0.03	0.13	0.10	0.30	0.16	0.01	0.17	0.46	
LMO-H1	3.30	9.94	0.07	0.04	3.61	44.51	14.52	0.01	22.81	98.81	0.83
1-σ	0.29	0.37	0.01	0.01	0.06	2.05	0.38	0.02	2.74	0.68	
LMO-H3	3.31	10.28	0.06	0.08	4.14	45.04	14.47	0.01	21.31	98.70	0.83
1-σ	0.37	0.18	0.01	0.01	0.19	0.44	0.40	0.01	0.84	0.29	
LMO-H4	2.52	10.62	0.04	0.06	6.41	44.66	13.95	0.01	20.27	98.54	0.95
1-σ	0.29	0.08	0.01	0.01	0.16	0.41	0.35	0.01	0.61	0.18	

1-σ is based on 10-15 repeated analyses.

Table S-4 Major and minor elements of plagioclase (in wt. %).

Run No.	TiO_2	CaO	K_2O	Na_2O	MgO	SiO_2	Al_2O_3	MnO	FeO_{tot}	Total	An
LMO-1	0.02	19.66	0.01	0.18	0.31	43.78	35.97	0.01	0.62	100.55	0.98
	0.01	0.18	0.01	0.02	0.10	0.45	0.42	0.02	0.08	0.16	
LMO-3	0.04	19.23	0.01	0.21	0.54	44.80	33.88	0.01	0.67	99.40	0.97
	0.00	0.19	0.01	0.03	0.08	0.40	0.31	0.01	0.10	0.25	
LMO-4	0.02	19.47	0.02	0.26	0.28	43.79	35.65	0.00	0.64	100.13	0.97
	0.01	0.15	0.00	0.03	0.05	0.25	0.21	0.01	0.08	0.20	
LMO-6	0.02	19.27	0.01	0.26	0.36	44.02	35.58	0.00	0.55	100.08	0.97
	0.01	0.17	0.01	0.04	0.05	0.42	0.57	0.00	0.07	0.30	
LMO-8	0.02	19.27	0.02	0.24	0.23	43.39	35.27	0.01	0.63	99.07	0.98
	0.01	0.22	0.01	0.03	0.04	0.41	0.45	0.00	0.05	0.40	
LMO-9	0.13	18.18	0.02	0.12	0.55	48.40	32.57	0.01	0.36	100.34	0.97
	0.10	0.24	0.01	0.01	0.12	0.60	0.42	0.01	0.21	0.45	
LMO-11	0.05	18.93	0.02	0.13	0.37	47.03	33.34	0.01	0.47	100.35	0.98
	0.01	0.19	0.01	0.01	0.03	0.50	0.37	0.01	0.05	0.34	
MORB-3	0.05	8.89	0.12	6.51	0.07	55.52	27.52	0.01	0.24	98.92	0.56
	0.01	0.21	0.01	0.14	0.01	0.52	0.20	0.01	0.06	0.41	
LMO-H1	0.03	19.45	0.03	0.14	0.24	44.17	35.88	0.01	0.55	100.49	0.98
	0.01	0.20	0.01	0.01	0.04	0.34	0.41	0.02	0.09	0.31	
LMO-H3	0.02	19.22	0.02	0.27	0.23	43.77	35.33	0.01	0.56	99.44	0.97
	0.01	0.16	0.01	0.03	0.02	0.18	0.25	0.01	0.07	0.38	
LMO-H4	0.04	19.44	0.02	0.15	0.32	43.56	35.38	0.01	0.75	99.66	0.98
	0.01	0.24	0.01	0.03	0.06	0.36	0.58	0.01	0.09	0.35	

1-σ is based on 10-15 repeated analyses.

Supplementary Figures

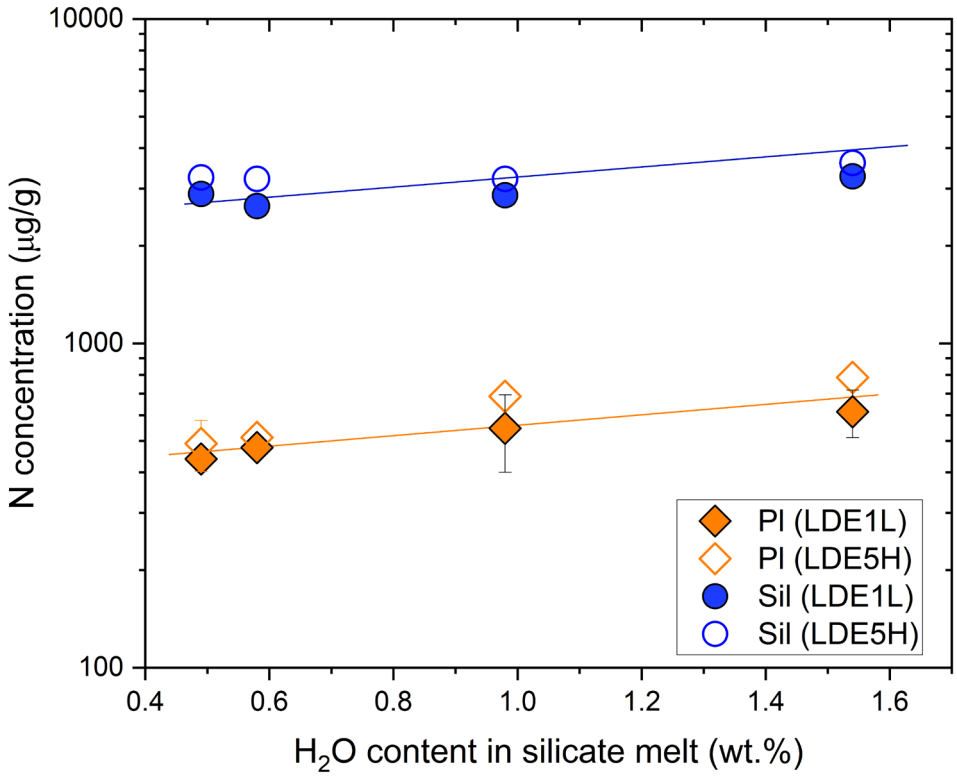

Figure S-1 N concentrations in plagioclase (Pl) and silicate melt (Sil) as a function of water content in silicate melt at 1 GPa and 1200 °C. N concentrations were measured using two different electron microprobes with an LDE1L and an LDE5H diffracting crystal, respectively.

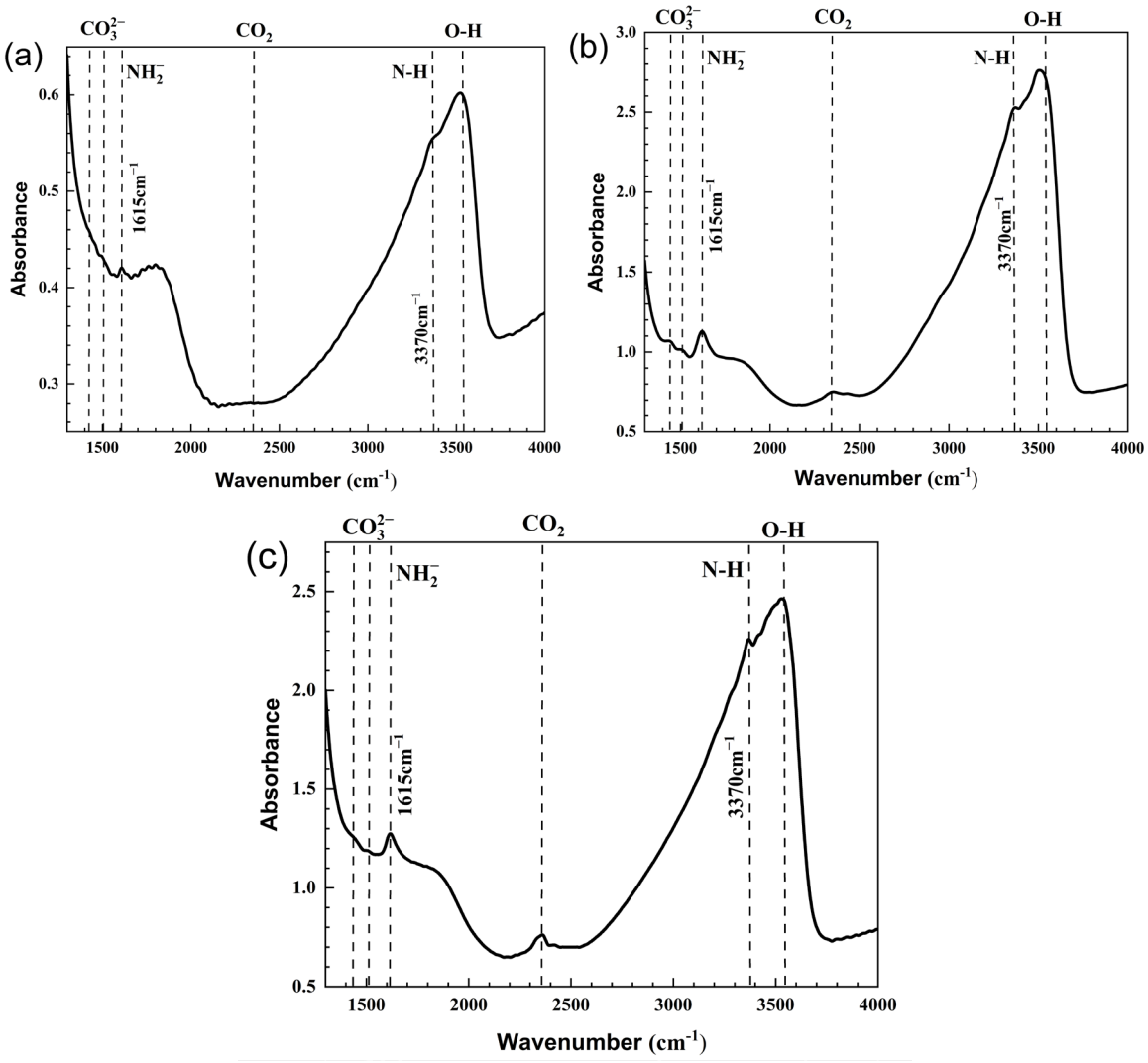

Figure S-2 FTIR spectral of quenched silicate melts. **(a)** Sample LMO-8 with 2890 µg/g N and 0.5 wt. % water. **(b)** Sample LMO-H1 with 3270 µg/g N and 1.5 wt. % water. **(c)** Sample LMO-H3 with 2860 µg/g N and 0.98 wt. % water. The peaks at 1615 and 3370 cm^{-1} were ascribed to N–H species (Armstrong *et al.*, 2015; Mosenfelder *et al.*, 2019). Note that the silicate melt of the nominally water-free sample LMO-8 contained 0.5 wt. % water.

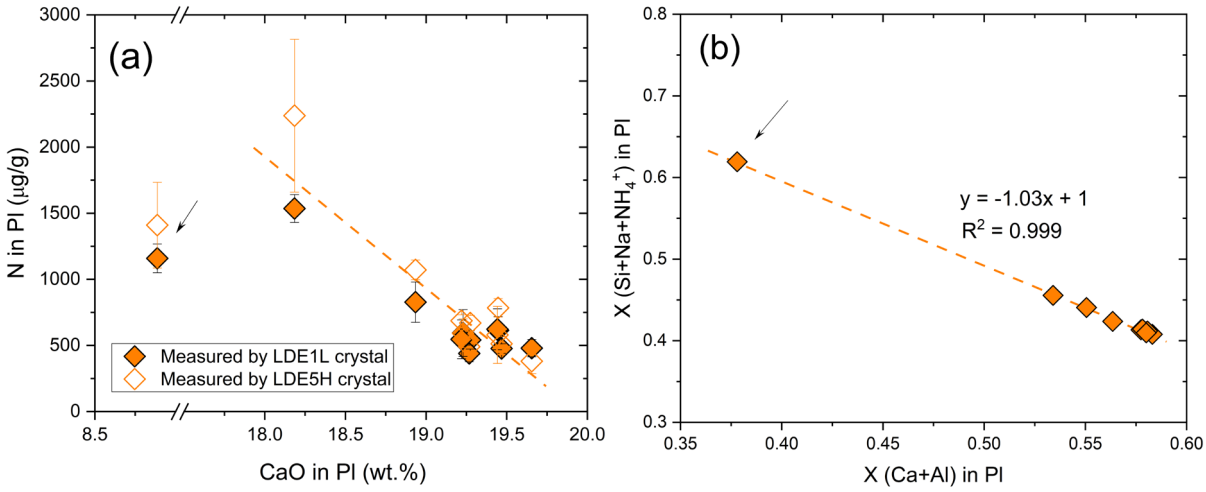

Figure S-3 The correlations between N and major elements in plagioclase (Pl). **(a)** N and CaO contents in plagioclase are negatively correlated, except one sample with significant Na_2O, as indicated by the arrow. **(b)** Mole fractions of (Ca+Al) *vs.* (Si+Na+NH_4^+) for all Pl samples are negatively correlated. The slope is consistent with a coupled substitution of $NH_4^+ + Na^+ + Si^{4+}$ for $Ca^{2+} + Al^{3+}$ in plagioclase.

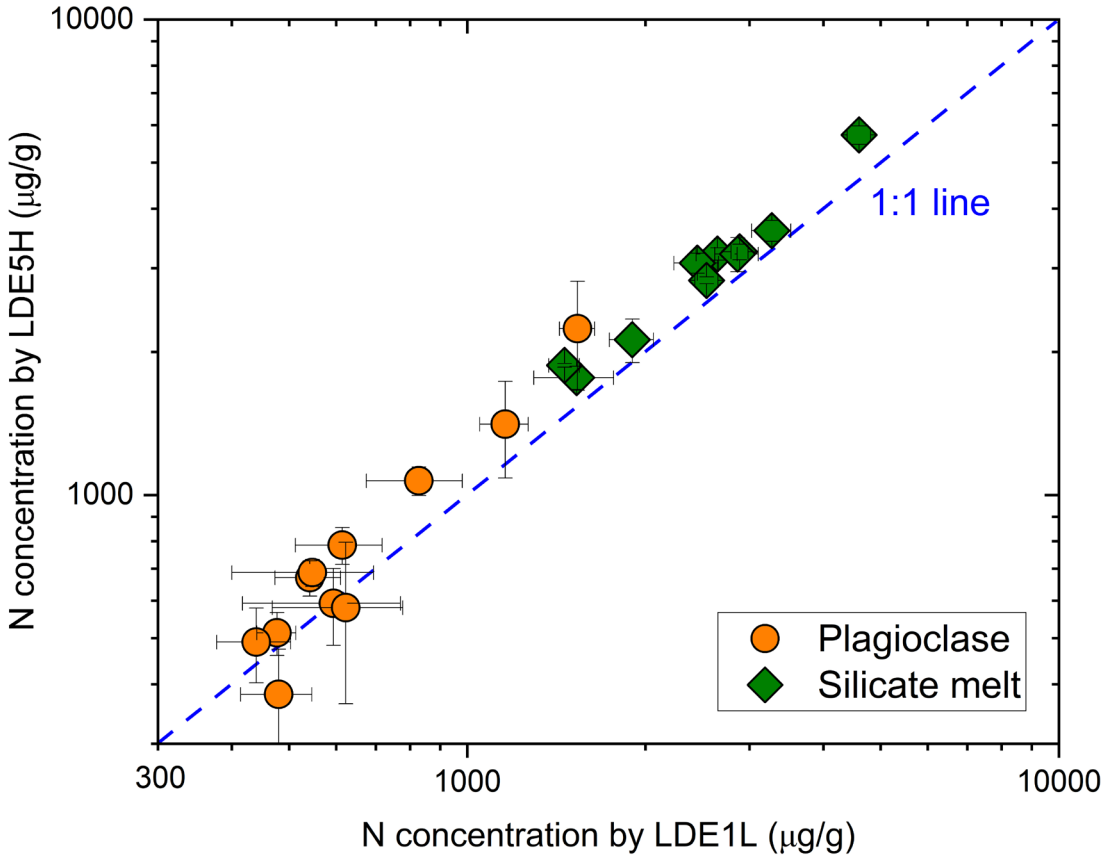

Figure S-4 Comparison of N concentrations in plagioclase and silicate melt measured using LDE1L and LDE5H crystal.

Supplementary Information References

Armstrong, L.S., Hirschmann, M.M., Stanley, B.D., Falksen, E.G., Jacobsen, S.D. (2015) Speciation and solubility of reduced C–O–H–N volatiles in mafic melt: Implications for volcanism, atmospheric evolution, and deep volatile cycles in the terrestrial planets. *Geochimica et Cosmochimica Acta* 171, 283-302. https://doi.org10.1016/j.gca.2015.07.007

Beran, A., Armstrong, J., Rossman, G.R. (1992) Infrared and electron microprobe analysis of ammonium ions in hyalophane feldspar. *European Journal of Mineralogy* 4, 847-850.

Cui, J.-Q., Yang, S.-Y., Jiang, S.-Y., Xie, J. (2019) Improved Accuracy for Trace Element Analysis of Al and Ti in Quartz by Electron Probe Microanalysis. *Microscopy and Microanalysis* 25, 47-57. https://doi.org10.1017/s1431927618015672

Donovan, J.J., Lowers, H.A., Rusk, B.G. (2011) Improved electron probe microanalysis of trace elements in quartz. *American Mineralogist* 96, 274-282. https://doi.org10.2138/am.2011.3631

Gao, Z., Yang, Y.-N., Yang, S.-Y., Li, Y. (2022) Experimental determination of N_2 solubility in silicate melts and implications for N_2–Ar–CO_2 fractionation in magmas. *Geochimica et Cosmochimica Acta* 326, 17-40. https://doi.org10.1016/j.gca.2022.04.001

Hamada, M., Ushioda, M., Fujii, T., Takahashi, E. (2013) Hydrogen concentration in plagioclase as a hygrometer of arc basaltic melts: Approaches from melt inclusion analyses and hydrous melting experiments. *Earth and Planetary Science Letters* 365, 253-262. https://doi.org10.1016/j.epsl.2013.01.026

Holzheid, A., Palme, H., Chakraborty, S. (1997) The activities of NiO, CoO and FeO in silicate melts. *Chemical geology* 139, 21-38.

Jackson, C.R.M., Cottrell, E., Andrews, B. (2021) Warm and oxidizing slabs limit ingassing efficiency of nitrogen to the mantle. *Earth and Planetary Science Letters* 553. https://doi.org10.1016/j.epsl.2020.116615

Jing, J.-J., Berndt, J., Klemme, S., van Westrenen, W. (2024) Fluorine abundance of the lunar magma ocean constrained by experimentally determined mineral-melt F partitioning. *Geochimica et Cosmochimica Acta* 364, 89-99. https://doi.org10.1016/j.gca.2023.11.011

Li, Y., Dasgupta, R., Tsuno, K. (2017) Carbon contents in reduced basalts at graphite saturation: Implications for the degassing of Mars, Mercury, and the Moon. *Journal of Geophysical Research: Planets* 122, 1300-1320. https://doi.org10.1002/2017je005289

Li, Y., Huang, R., Wiedenbeck, M., Keppler, H. (2015) Nitrogen distribution between aqueous fluids and silicate melts. *Earth and Planetary Science Letters* 411, 218-228.

Lin, Y., Tronche, E.J., Steenstra, E.S., van Westrenen, W. (2017) Evidence for an early wet Moon from experimental crystallization of the lunar magma ocean. *Nature Geoscience* 10, 14-18. https://doi.org10.1038/ngeo2845

Ma, Z. (2001) Thermodynamic description for concentrated metallic solutions using interaction parameters. *Metallurgical and Materials Transactions B* 32, 87-103.

Mallik, A., Li, Y., Wiedenbeck, M. (2018) Nitrogen evolution within the Earth's atmosphere-mantle system assessed by recycling in subduction zones. *Earth and Planetary Science Letters* 482, 556-566. https://doi.org10.1016/j.epsl.2017.11.045

Mare, E.R., Chen, J., Buisman, I., Hayward, C., Burnham, A.D., Melai, C., Stüeken, E.E., Bromiley, G., Mikhail, S. (2025) Problems and Solutions when Quantifying Nitrogen in Silicate and Oxide Minerals and Glasses Using Electron Probe Microanalysis. *Geostandards and Geoanalytical Research*. https://doi.org10.1111/ggr.12605

Mosenfelder, J.L., Von Der Handt, A., Füri, E., Dalou, C., Hervig, R.L., Rossman, G.R., Hirschmann, M.M. (2019) Nitrogen incorporation in silicates and metals: Results from SIMS, EPMA, FTIR, and laser-extraction mass spectrometry. *American Mineralogist* 104, 31-46. https://doi.org10.2138/am-2019-6533

O'Neill, H.S.C., Eggins, S.M. (2002) The effect of melt composition on trace element partitioning: an experimental investigation of the activity coefficients of FeO, NiO, CoO, MoO_2 and MoO_3 in silicate melts. *Chemical Geology* 186, 151-181.

von der Handt, A., Mosenfelder, J., Dalou, C., Hirschmann, M.M. (2019) Recent advances in the analysis of nitrogen by epma. *Microscopy and Microanalysis* 25, 2320-2321. https://doi.org10.1017/s1431927619012339

Wood, B.J., Li, J., Shahar, A. (2013) Carbon in the core: its influence on the properties of core and mantle. *Rev Mineral Geochem* 75, 231-250.

Yamashita, S., Kitamura, T., Kusakabe, M. (1997) Infrared spectroscopy of hydrous glasses of arc magma compositions. *Geochemical Journal* 31, 169-174. https://doi.org10.2343/geochemj.31.169

Yang, S.-Y. (2022) Electron Probe Microanalysis In Geosciences: Analytical Procedures And Recent Advances. *Atomic Spectroscopy* 43. https://doi.org10.46770/as.2021.912

Yang, Y., Huang, W., Qi, Z., Xia, Q. (2022) Nitrogen Retention in Feldspar: Implications for Nitrogen Transport in Subduction Zones. *Journal of Geophysical Research: Solid Earth* 127, e2021JB023347. https://doi.orghttps://doi.org/10.1029/2021JB023347

Zhang, R.X., Yang, S.Y. (2016) A Mathematical Model for Determining Carbon Coating Thickness and Its Application in Electron Probe Microanalysis. *Microscopy and Microanalysis* 22, 1374-1380. https://doi.org10.1017/s143192761601182x